ACS Catalysis

Open Access

pubs.acs.org/acscatalysis

Research Article

Transient Surface Degradation of LSCO and LSFO during OER in Alkaline Electrolyte under Dynamic Cycling Conditions

Anton Kaus,* Bixian Ying, Zhenjie Teng, Muzaffar Maksumov, Lisa Heymann, Michael Merz, Stefan Schuppler, Peter Nagel, Florian Hausen, Karin Kleiner, and Felix Gunkel

Cite This: *ACS Catal.* 2025, 15, 13768−13777

Read Online

ACCESS | Metrics & More | Article Recommendations | Supporting Information

ABSTRACT: A fundamental understanding of the relationship between activity and stability is essential for rationalizing materials used as catalysts for the oxygen evolution reaction (OER). In the case of oxide perovskites, the catalytic activity of OER catalysts is often linked to the electronic structure, such as the degree of hybridization and occupation of the O 2p and transition metal 3d orbitals (TM 3d−O 2p), but their transient behavior during catalyst lifetime and degradation remains poorly understood. To address this, an epitaxial model system approach is utilized, comparing $La_{0.6}Sr_{0.4}CoO_{3-\delta}$ (LSCO) and $La_{0.6}Sr_{0.4}FeO_{3-\delta}$ (LSFO) as model OER catalysts. Both materials show distinctly different degradation mechanisms under dynamic cycling, namely a surface-passivation-mediated degradation in LSFO and an extended bulk degradation in LSCO. This contrasting behavior is consistently observed in their postcatalysis morphology, crystallinity, electronic structure, and electrochemical redox behavior. Our findings indicate a correlation between the hosted transition metal and the dominant degradation mechanism. This relationship leads to distinct transient behaviors of electronic structure, morphology, and OER activity. It also indicates a systematic loss of available hybrid electronic states over the catalyst's lifetime.

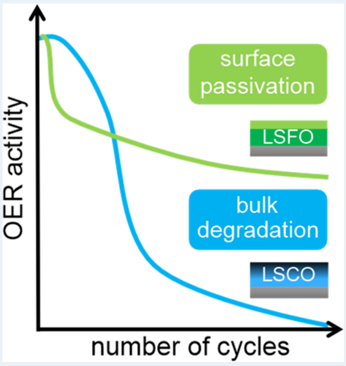

KEYWORDS: *oxygen evolution reaction, alkaline electrolyte, perovskite oxides, stability, X-ray absorption spectroscopy, model catalyst, in-operando atomic force microscopy, electrolysis*

■ INTRODUCTION

Perovskite oxides serve as excellent building blocks for fine-tuning the electronic structure of electrocatalysts, which can be achieved, for example, through B-site substitution.[1,2] This degree of freedom allows for a correlation between the electronic structure and the activity-stability relationship of the electrocatalyst.[3−6] In the case of water electrolysis in an alkaline environment, perovskite oxides are particularly suitable as anode materials to catalyze the sluggish oxygen evolution reaction (OER).[7−9] The OER requires a high overpotential and, thus, is currently more critical for efficient water-splitting processes than the hydrogen evolution reaction.[9−11] However, the limited stability of the perovskite oxides remains an issue. Prolonged usage leads to degradation, such as amorphization of the crystalline phase and dissolution of the transition metal or lanthanide/alkaline-earth metal.[12−14] Various engineering approaches to control the activity-stability relationships were developed to overcome these limitations.[6] These approaches include characterizing surface changes through *in-operando* atomic force microscopy (AFM) in tailored electrochemical environments,[12] altering the catalysts' surface termination,[15] and conducting atomic engineering of the catalyst.[16−18] However, the detailed degradation mechanism reveals complex chemical behaviors and also greatly depends on how stability is tested. Weber et al. observed two distinct degradation mechanisms for $La_{0.6}Sr_{0.4}CoO_{3-\delta}$ (LSCO) under different electrochemical testing conditions, namely dynamic versus static loads.[19,20] Their findings indicate that dynamic loads can lead to a complete decomposition of the electrocatalyst, whereas static loads result in a surface reconstruction followed by passivation. This suggests that processes occurring at lower potentials during cycling may significantly influence the degradation behavior of the catalyst. The degradation processes are mainly attributed to the dissolution of alkaline-earth metals and transition metals, which may cause amorphization or surface reconstruction.[21] This understanding underscores the complexity of material behavior under varying operational conditions. Understanding these degradation mechanisms of perovskite oxides in alkaline electrolytes under dynamic conditions is crucial for optimizing electrolyzers' utility with a volatile energy supply by a rational materials design.

Received: April 2, 2025
Revised: July 14, 2025
Accepted: July 16, 2025

https://doi.org/10.1021/acscatal.5c02273
ACS Catal. 2025, 15, 13768−13777

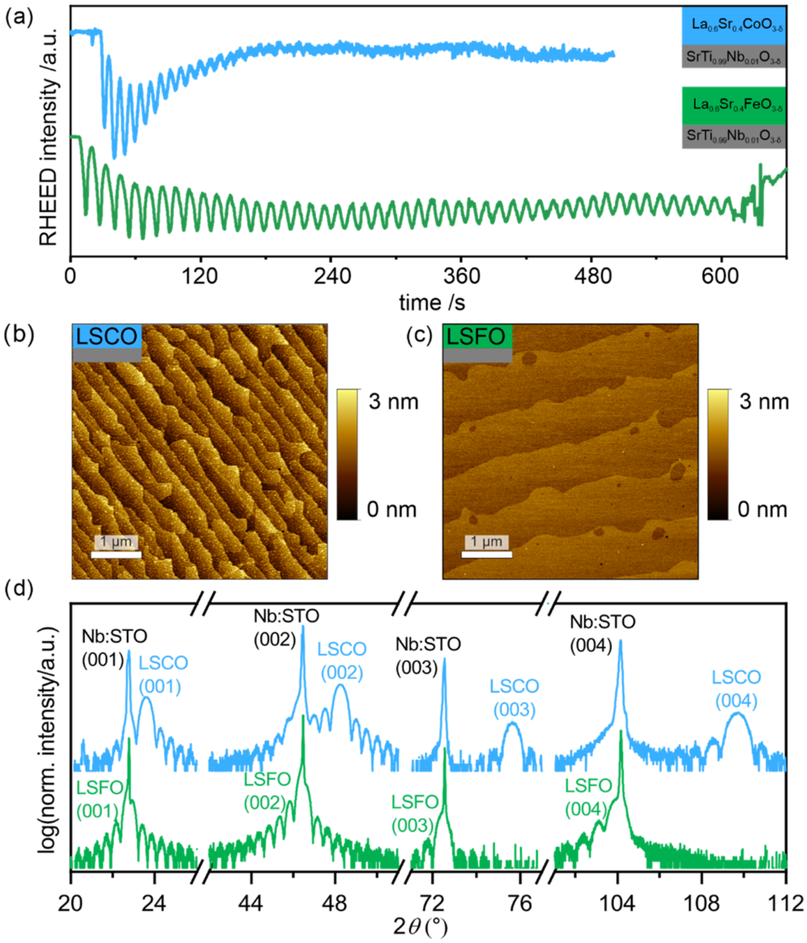

Figure 1. Epitaxial thin film catalysts' initial structural and morphological properties. (a) RHEED intensity during growth of the LSCO and LSFO model catalysts. (b) and (c) corresponding morphology visible in the AFM images of the as-grown samples. (d) X-ray diffractogram showing the epitaxial thin films of LSCO (blue) and LSFO (green) in (001) orientation grown on Nb:STO (001).

The hybridization of the transition metal and oxygen states near the Fermi level is a widely studied activity descriptor, as these states are directly involved in chemical bonding and electronic charge transfer during the OER.[11,22] In the soft X-ray regime, transition metal L edge spectra yield information about the transition metal's oxidation and spin states.[23−26] The unoccupied transition metal states hybridized with O 2p character (TM 3d−O 2p) are visible in the O *K*-edge spectra of the perovskite oxide.[27] Yet, the correlation between the degradation mechanism and the TM 3d−O 2p states remains unknown. A fundamental understanding of the transformations and transient behavior of the degraded electrocatalyst's electronic structure is essential for controlling and ultimately preventing the degradation mechanism. To address this, epitaxial thin films with well-defined surfaces and crystallinity provide an ideal basis for investigation.[21,28−30] The transient degradation can be investigated under similar structural conditions, allowing for a systematic comparison of the behavior of different TM-based OER catalysts.

In this study, we investigate how the electronic structure of pristine LSCO and LSFO thin films transforms under dynamic conditions in alkaline electrolyte. Two distinctly different degradation mechanisms were observed: surface passivation for LSFO and bulk degradation for LSCO. These findings were revealed through near-edge X-ray absorption fine structure (NEXAFS), *in-operando* atomic force microscopy (AFM), and X-ray diffraction (XRD). The degradation mechanism changes with the reversibility of the transition metal's oxidation state during cycling. Bulk degradation occurs with reversible changes in the oxidation state, while surface passivation is observed during a predominantly oxidizing process of the perovskite oxide during electrochemical cycling. The surface-limited degradation mechanism leads to stabilized OER activity after initial cycling. In contrast, bulk degradation is characterized by continuous losses in OER activity.

RESULTS AND DISCUSSION

Epitaxial model catalysts were synthesized by reflection high-energy electron diffraction (RHEED)-controlled pulsed laser deposition. Figure 1 shows the epitaxial thin film catalysts' initial structural and morphological properties. In Figure 1a the evolution of the RHEED intensity during the growth of LSCO and LSFO is displayed. Intensity oscillations were observed in both cases, indicating a layer-by-layer growth mode. In the case of LSCO the vanishing of the oscillations is due to the transition from layer-by-layer to step-flow-like growth mode, which has been previously observed for LSCO.[19] We further note that occasional step bunching can be induced from the substrates. Each oscillation corresponds to the deposition of a single monolayer of the desired perovskite oxide onto the niobium-doped strontium titanate (Nb:STO) substrate. Both depositions result in a catalyst film that is 20 nm, consisting of

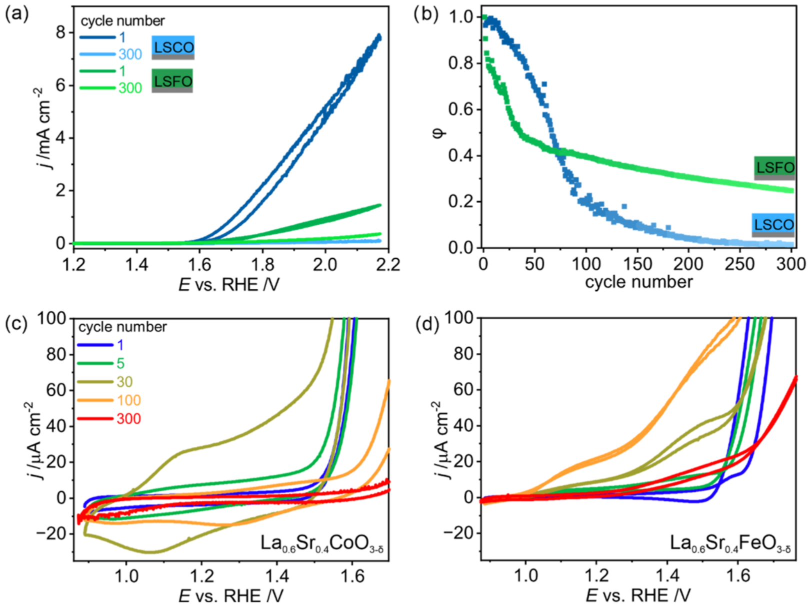

Figure 2. (a) First and 300th cyclic voltammogram of LSCO and LSFO in 0.1 M KOH with a sweep rate of 10 mV/s up to a maximum potential of 2.2 V vs RHE. The dark lines are the initial sweeps, and the light-colored lines are the 300th cycle. (b) Ratio of the current density at 2.2 V vs RHE of each cycle n ($j_n^{\max}$) to the initially reached current density ($j_1^{\max}$) for LSCO (blue) and LSFO (green). Zoomed-in area of the cyclic voltammogram of LSCO (c) and LSFO (d) for the starting potentials of the cyclic voltammetry measurement for various cycle numbers.

either LSCO or LSFO on the single crystal substrate. The morphology of the as-grown thin films is examined by AFM, as shown in Figure 1b,c. The typical step terraces of the underlying substrate remain visible in both materials, indicating homogeneous growth. The root-mean-square (RMS) roughness of the as-grown state of the thin films is 0.5 and 0.19 nm for LSCO and LSFO, respectively. Note that the RMS value for the LSCO is higher due to step bunching present in the substrate (RMS value: 0.47 nm), and the LSCO thin film itself smoothly covers the substrate.

Figure 1d shows the X-ray diffractograms of the as-grown thin film catalysts. The sharp peaks correspond to the Nb:STO substrate, and in the case of the LSCO, the thin film peaks are visible toward higher angles with intensity oscillations on both sides. For LSFO, the thin film peaks overlap with the substrate peaks but are clearly evident by the intensity shoulder (most noticeable around (004) reflection) toward lower angles and clear thickness oscillations. The visible Laue oscillations in both cases indicate the well-defined substrate-to-thin-film interface and surface. The period of these oscillations confirms the thickness of the catalyst thin films to be around 20 nm. Hence, the model catalysts have a single crystalline nature with a defined crystallographic orientation. These highly defined model catalysts with the same crystallographic orientation serve as the starting point to further understand the degradation behavior of perovskite oxides under dynamic conditions in alkaline electrolyte and to disentangle the influence of morphology and chemistry.

For electrochemical experiments, 50 nm of platinum was sputtered around the thin films (backside, edges, and front edges). The sputtered thin films were then investigated using a rotating disk electrode setup and repeatedly cycled between 0.9 and 2.2 V vs a reversible hydrogen electrode (RHE) to mimic the degradation under dynamic loads in a fixed potential window. The following potentials are all in reference to the RHE. Four samples for each material were investigated in this manner and cycled for 5, 30, 100, and 300 cycles to understand the transient degradation of LSCO and LSFO.

Figure 2 displays the typical current density as a function of the applied potential of the model catalysts in 0.1 M KOH. Figure 2a shows the cyclic voltammogram (CV) of LSCO and LSFO for the initial cyclic sweep (dark color) and the 300th cyclic sweep (light color) up to 2.2 V. Note that *iR* corrections were not applied to the data, as the uncompensated resistance obtained from the impedance measurements continuously increased with enhanced cycle number (cf. Figure S1). Significant current densities are achieved at potentials above 1.6 V for LSCO, which rises sharply with increased potential to a final value of about 8 mA cm^{-2} at 2.2 V.

In the case of LSFO, the current increase is less pronounced with applied potential and reaches a maximum of about 1.5 mA cm^{-2} at 2.2 V. Repeated cycling of the applied potential up to 2.2 V for 300 times resulted in a significant reduction in the maximum current density achieved per cycle. The light colors in Figure 2a show the 300th cycle of LSCO (light blue) and LSFO (light green). For LSCO, the maximum current density achieved per cycle dropped to 0.1 mA cm^{-2}, which corresponds to a decrease by a factor of 80. For LSFO, the current density after 300 cycles resulted in a final current density of 0.36 mA cm^{-2} and, therefore, a reduction by a factor of 4.

Figure 2b illustrates this trend by plotting the ratio, $\varphi = j_n^{\max}/j_1^{\max}$, of the current density at 2.2 V achieved at cycle number n ($j_n^{\max}$) with respect to the initial value during the first cycle ($j_1^{\max}$). For LSCO, φ shows a low initial negative slope, indicating a slight loss of activity. After the first 5 cycles, the current density remains above 95% of its initial value. However, continuous cycling leads to a significant decline in the current densities, which can be seen by the steep slope in Figure 2b. After around 30 cycles, φ significantly decreases and continuously declines until around the 100th cycle, at which point only about 20% of the initial current density is retained.

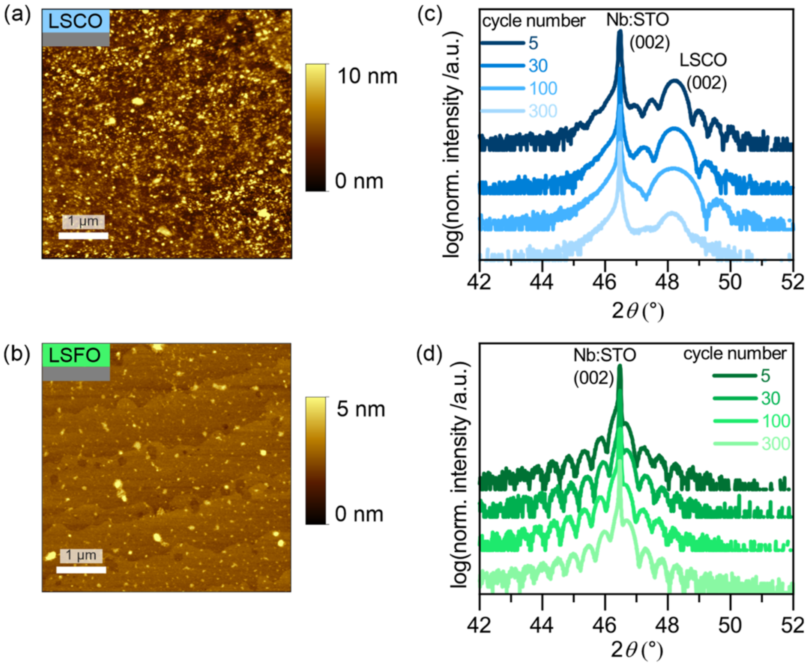

Figure 3. (a, b) Atomic force microscopy images of the catalysts post 300 cycles in 0.1 M KOH for LSCO and LSFO, respectively. (c, d) The corresponding diffractograms of the LSCO (blue) and LSFO (green) thin films.

Although the rate of decay slows down afterward, a nearly complete loss of activity occurs over the subsequent 200 cycles.

LSFO exhibits a distinctly different behavior regarding φ. Initially, there is a sharp decline in current density, with an observed decrease of about 20% after 5 cycles. Continued cycling leads to further reduction; however, the OER activity of LSFO stabilizes after approximately 40 cycles at a ratio of 0.47. After 300 cycles, φ drops to about 0.25. Thus, while LSFO shows lower initial OER activity, its stabilization with repeated cycling ultimately leads to a higher current density than for LSCO after 300 cycles. Note that leaching of the transition metals into the electrolyte can have an influence on catalytic activity and stability.[31,32] Our measurements were carried out in an electrochemical cell with a volume of 100 mL, which makes a potential impurity concentration due to leaching very small, yet a residual influence, e.g., of dissolved Fe species, cannot be excluded.

Figure 2c,d show the corresponding cyclic voltammogram during the degradation of each LSCO and LSFO catalyst at low applied potentials, in which the intrinsic redox behavior of the catalysts can be observed. It is found that redox reactions start to emerge with an increased number of cycles. During dynamic cycling, two features can be observed in the case of LSCO: (1) oxidation features during the anodic sweep and (2) reduction features during the cathodic sweep. This indicates a dynamic process of oxidation and reduction on the surface of the Co-containing catalyst. The concrete oxidation state of Co is difficult to determine from the CVs alone; however, we can see a qualitative trend in the kinetics of the redox reaction. The peak height first increases in the initial cycles but then reduces at a higher number of cycles and is almost completely gone after 300 cycles. LSFO, on the other hand, shows primarily signatures of oxidation, while reduction features are hardly observed during cycling (Figure 2d). For LSFO, an increase in current density at lower potentials is observed during both the anodic and cathodic sweeps with each cycle. This indicates that an oxidation reaction occurs, but with a much less pronounced reduction during the cathodic sweep in the here employed potential window. Reduction peaks observed in LSFO are observed at potentials below 0.8 V vs RHE.[33] Moreover, byproduct reactions, such as hydrogen peroxide, may contribute to the observed behavior during cycling.[34,35] Therefore, it appears that LSFO continuously undergoes oxidation until it reaches saturation at around 300 cycles. In contrast, LSCO undergoes dynamic cycles of consecutive oxidation and reduction processes.

To understand the distinctly different degradation and redox behavior in more detail, the thin film properties were revisited after the electrochemical processing. Figure 3a shows the resulting morphology of the LSCO catalyst after 300 cycles in 0.1 M KOH after removing the sample from the RDE, followed by gentle cleaning and drying. The step-terraces that were evident in the as-grown state are not distinguishable anymore. This indicates a significant change in the surface structure of the catalyst, which is also reflected in the increased RMS value of 1.86 nm.

In contrast, LSFO still shows a step-terrace structure (Figure 3b), and only a small residue appears on the surface after 300 cycles, increasing the RMS value only slightly to 0.61 nm. In addition, X-ray diffraction was employed on the degraded catalysts. Figure 3c shows the diffractograms for the LSCO catalyst after various number of cycles, from 5 cycles (dark blue) up to 300 cycles (light blue). The initially observed Laue oscillations vanished, which is in line with the observed roughening of the catalyst surface. The LSCO (002) peak exhibits reduced intensity and becomes slightly broader, indicating a loss of crystallinity and an enhanced level of disorder within the entire 20 nm thick film. This observation is consistent with previous work showing a complete loss of the crystalline perovskite phase for degraded LSCO catalysts after 30 CV cycles with higher current densities.[19] In contrast to the initial lattice expansion observed at higher current densities,[19] we observe a stable lattice parameter of the LSCO layer upon degradation.

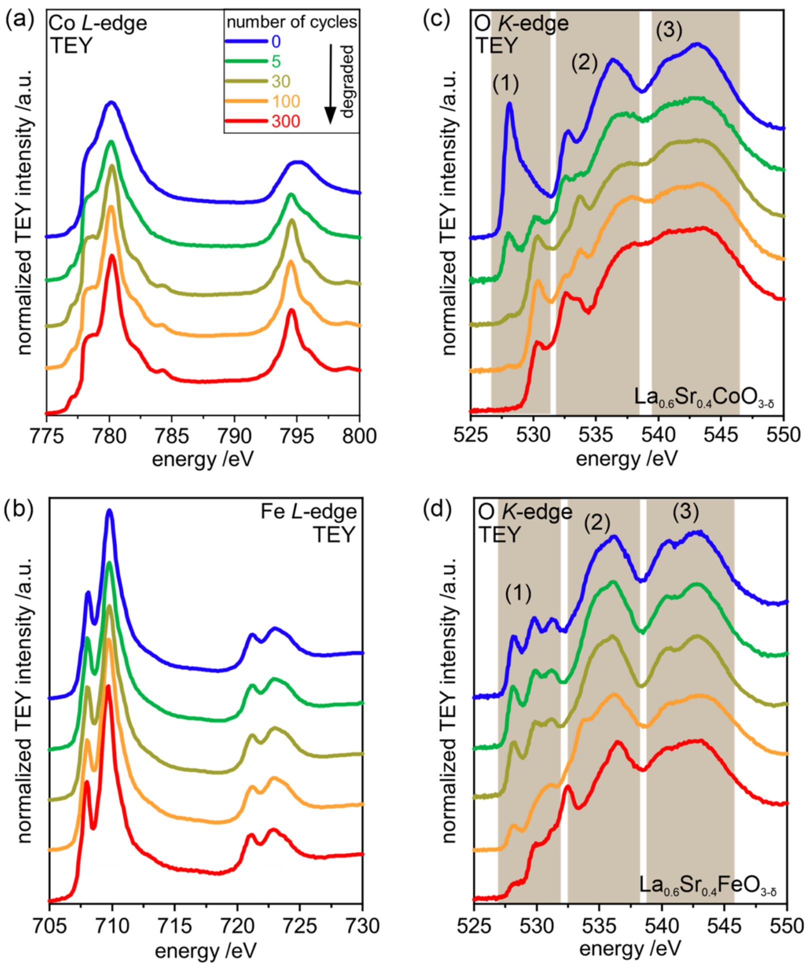

Figure 4. (a) Evolution of the normalized Co $L_{2,3}$ NEXAFS spectra of LSCO after increased number of cycles. (b) Evolution of the normalized Fe $L_{2,3}$ NEXAFS spectra of LSFO after increased number of cycles. (c) Evolution of the normalized O *K* NEXAFS spectra of the same samples as in (a). (d) Evolution of the normalized O *K* NEXAFS spectra of the same samples as in (b).

In contrast to the behavior of LSCO, LSFO shows almost no change in the crystal structure after 300 cycles (Figure 3d). The Laue oscillations remain after the electrochemical treatment, consistent with the primarily smooth and single-crystal-like surface observed through AFM. While both LSCO and LSFO initially exhibit comparable single crystalline and atomically smooth epitaxial characteristics, they follow distinctly different degradation mechanisms under dynamic loads. LSCO loses its crystallinity and initial morphology, whereas LSFO remains structurally almost unchanged after the OER. Based on the Laue oscillations in the XRD data, the difference in the crystalline layer thickness of LSFO after 300 cycles is around 0.4 nm, which corresponds to a reduction by one unit cell of the perovskite oxide. Therefore, it appears that the passivation layer on the surface is only very thin in the case of LSFO, preserving the bulk structure of the catalyst. The XRD analysis did not reveal any secondary phases. However, it is possible that a nanometer thin surface layer could be below the resolution limit of X-ray diffraction.

To monitor changes in the electronic structure of the OER catalysts following repeated cycling, we employed X-ray absorption spectroscopy (XAS). The samples were cycled several times, as indicated, and measured using soft X-rays. All samples consistently showed the characteristic degradation behavior discussed in Figure 2a,b (see Figure S2). The spectra were recorded simultaneously in fluorescence yield (FY) for bulk properties and total electron yield (TEY) mode to enhance surface sensitivity.

Figure 4a shows the Co $L_{2,3}$-edge X-ray absorption spectra of the LSCO catalyst after different cycling numbers obtained in TEY. The spectra of the as-grown catalyst (blue) show the L_3 edge at 780 eV with a shoulder on the lower energy side and the L_2 edge at 795 eV. The broader peaks in the as-grown state rapidly transition into much sharper spectral features, evident already after 5 CV cycles. As discussed in ref,[24] a broad spectral feature in the Co *L*-edge indicates a high spin state for Co^{3+}, while sharper and more defined shapes indicate a low spin state and more ionic bonding. The L_3 edge at around 780 eV shows a shoulder at 778 eV, which indicates a nominal Co^{2+} contribution that becomes more defined with an increased number of cycles.[23] This valence state has been reported in the literature for LSCO upon reduction and thus supports the existence of Co^{2+} in similar structures.[36] At the same time, however, the Co^{2+} contribution is less pronounced in the bulk (see Figure S4) than in the surface-sensitive TEY mode NEXAFS spectra. Therefore, this valence state may be related to an extended surface species forming on LSCO while degrading, which is evident in the AFM and XRD measurements post cycling. As a result, the surface appeared to be more reduced and transitioned from a more covalent to ionic

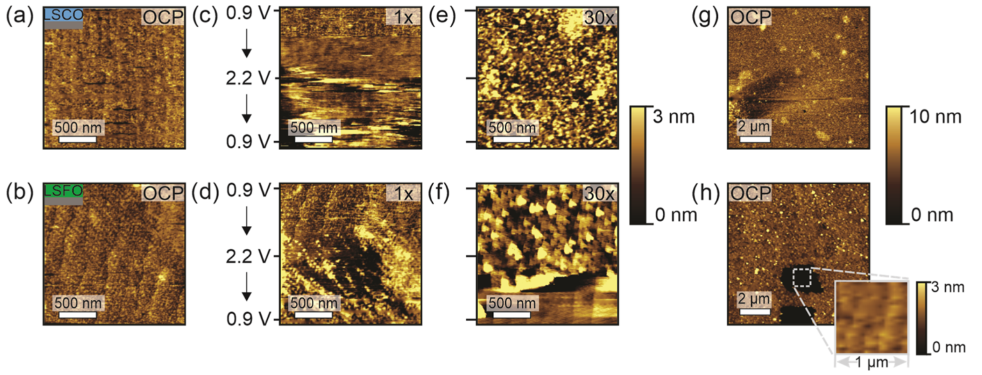

Figure 5. *In-operando* AFM topography of LSCO and LSFO during electrochemical cycles as indicated with an applied normal load of 5 nN. (a, b) at OCP; (c, d) during the first CV; (e-f) during the 30th CV; (g, h) at OCP, zoomed out after 30 CVs, respectively.

structure after cycling. This observation is consistent with previously reported reduced Co valence at the surface of LSCO catalysts.[20] At large cycle numbers, similar spectral changes of the Co *L*-edge were also observed in FY spectra (see Figure S4a), indicating that the reduction and loss of covalency occur within the entire LSCO layer. It is important to note that cobalt dissolution during electrochemical testing may contribute to the deactivation of the catalyst. However, the Co *L*-edge analysis of the degraded catalysts confirms that cobalt is still present on the surface. The observed spectral changes indicate an increased amorphous character compared to the initial state. XRD analysis shows that the crystalline portion of the catalyst layer has diminished in thickness following aging, while the substrate remains covered. Under static degradation conditions, mainly strontium dissolution was observed, with minimal cobalt dissolution detected.[20]

Figure 4b shows the Fe $L_{2,3}$ NEXAFS spectra of the LSFO thin film after the same number of cycles as for the LSCO thin film. In contrast to LSCO, only minor changes in spectral shape are visible even after 300 cycles, which indicates that the oxidation state of the iron hardly changes with increased number of cycles. Consistently stable Fe *L*-edge spectra were also observed in FY probing the entire thin film (cf. SI Figure S4b).

The O *K*-edge was recorded to further correlate the decay of the activity after repeated cycles with transient changes in the electronic structure of the model catalysts. Figure 4c,d show the TEY O *K*-edges of the LSCO and LSFO catalysts with an increased number of cycles. Three characteristic energy regions can be defined from lowest to highest energy depending on the involved orbitals: (1) TM 3d−O 2p centered at around 528 eV, (2) Sr 4d−O 2p/La 5d−O 2p centered at around 537 eV, and (3) TM 4sp−O 2p centered at around 544 eV.

For LSCO, the prepeak at 528 eV decreases dramatically within the first 5 cycles and entirely vanishes after 300 cycles, correlating with a decrease in unoccupied TM 3d t_{2g}−O 2p hybrid states.[37] The feature at 530 eV corresponds to unoccupied O 2p states hybridized with Co 3d e_g states which become visible after 5 cycles.[37] Given the TEY's information depth, and respective energy range, an influence of the STO substrate is unlikely, which is confirmed by the O *K*-edge measurement of STO provided in the Supporting Information (Figure S5). Furthermore, the spectral features observed at higher photon energies show a general broadening. This loss of fine structure features at higher energies in the O *K*-edge may indicate the loss of crystal coherence during electrochemical cycling. This may ultimately be identified with an amorphization of the catalyst within the TEY probing depth, which is a few nanometers from the surface.

Turning to LSFO, for which only marginal spectral changes were observed in the Fe *L*-edge, the loss of activity observed in the electrochemical characterization (Figure 2b), can be correlated to similar spectral features in the O *K*-edge as for LSCO. The first region is now representing the hybridization of the Fe 3d−O 2p states. The first peak corresponds to the $e_g\uparrow$ state followed by the $t_{2g}\downarrow$ and $e_g\downarrow$ states toward higher energy.[22] The peak intensity follows a similar trend as the LSCO catalyst. The prepeak intensity decreases with an increased number of cycles. However, the decay in intensity is much less pronounced than in the LSCO case. For LSFO, even after 300 cycles, a nonvanishing prepeak intensity can be seen at 528 eV, which means the electronic structure of the LSFO catalyst still exhibits features from the as-grown state. In addition, the TEY O *K*-edge spectra of LSFO after 300 cycles exhibits new features that appear around 533 and 537 eV. This suggests a shift in the chemical environment surrounding the oxygen atoms, potentially indicating a chemical phase transformation near the catalyst's surface.[38]

For both materials, the prepeak in the O *K*-edge decreases with an increasing number of cycles, indicating a reduced concentration of initially empty states. The availability of these states may have changed due to either a loss of hybridization or occupation of the states. As a result, the empty states are no longer available to participate in the OER, and electron transfer is hindered. However, the extent of the decrease in the peak varies, much like the differences observed in the cyclic voltammograms. For LSCO, these states are lost after the first 30 cycles on the surface and continuously disappear in the bulk after 100 cycles (Figure S4c), which corresponds to the observed continuous drop in activity of the cobalt-containing catalyst. While for LSFO, the FY data (Figure S4d) indicates only negligible losses in the bulk even after 100 cycles, supporting the preservation of the bulk structure.

These changes in the X-ray absorption spectra, depending on the information depth, support the idea of a surface phase degradation for the LSFO catalyst and a bulk degradation for the LSCO catalyst. These varying observations, depending on the specific transition metal, highlight that the degradation mechanisms differ even under the same electrochemical treatment. We note that the concrete chemical species of the passive surface layer on the Fe-containing catalyst cannot be determined based on the present data set. Further experiments are needed to give a good estimate of the chemical nature of that layer. Moreover, A-site suboxides and hydroxides were reported to contribute to the surface passivation of perovskite OER catalysts.[20]

To analyze the surface during operation and observe the onset of degradation, we used contact mode *in-operando* AFM. Here, the model catalysts were investigated in the same 0.1 M KOH electrolyte within a three-electrode setup. Figure 5a,b show the initial surface morphology at open circuit potential (OCP) for LSCO and LSFO, respectively. During the first CV cycle between 0.9 and 2.2 V, surface changes occur in LSCO at about 1.4 V (Figure 5c) and in LSFO at around 1.7 V (Figure 5d), when approaching the OER regime. LSCO exhibits an initial surface degradation, becoming completely unrecognizable by the 30th CV cycle (Figure 5e).

In contrast, LSFO develops particle-like structures on its surface, which remain even when returning to lower potentials. Repeated cycling results in additional roughening and artifacts caused by tip degradation. Interestingly, a clean step terrace morphology is observed in neighboring regions (Figure 5f bottom), which may indicate that the AFM tip has partially removed the surface adlayer that formed on LSFO. Consistently, enlarging the scan area after 30 electrochemical cycles, LSCO's surface appears entirely degraded (Figure 5g), matching the ex situ AFM results (Figure 3a), while LSFO largely retains a particle-covered surface. The mechanical interaction in the contact mode, however, removed the adlayer of the previously scanned area. The enhanced contrast in Figure 5h highlights an intact step-terrace structure. The *in-operando* data indicates that the LSFO surface phase has weak bonding to the thin film and can be easily removed. This also confirms the distinctly different transient behavior and degradation mechanisms predominant in LSCO and LSFO.

CONCLUSIONS

In conclusion, LSCO and LSFO exhibit distinctly different degradation behaviors under dynamic potential cycling in alkaline electrolyte. The catalytic activity and stability of these perovskite oxides depend on their electronic structure, which in turn is influenced by the host transition metal. The Co-based LSCO catalyst demonstrates higher initial activity but undergoes significant bulk degradation, resulting in the loss of its initial crystalline structure, OER activity, morphology, and available hybrid TM 3d−O 2p electronic states. In contrast, LSFO initially shows lower activity but forms a passivation layer during operation, which reduces its activity while preventing further bulk degradation. Consequently, bulk-sensitive measurements, such as XRD and FY mode NEXAFS, show no changes after operation, while TEY mode NEXAFS and *in-operando* AFM show the formation of a passivation layer on the surface. The changes in both catalysts are irreversible, even at nonactive potentials. Yet, the facile mechanical removal of such a passivation layer could be an effective method for restoring catalyst activity. As a result, the choice of B-site cation affects the degradation mechanism, potentially enabling the stabilization of catalysts. For instance, a self-protecting catalyst made from iron and cobalt could retain the higher initial activity of Co-based catalysts while benefiting from the stability of Fe-based ones.

Overall, a surface passivation mechanism may be a more favorable degradation pathway than bulk decomposition, allowing for the possible recovery of catalysts through treatments that remove the passive layer. This emphasizes the importance of chemistry-dependent degradation pathways, that can be tuned and tailored by a careful catalyst design.

EXPERIMENTAL SECTION

Thin Film Fabrication. All thin film samples were grown on 0.5 × 10 × 10 mm^3 sized (001) oriented 0.5 wt % Nb-doped $SrTiO_3$ (Nb:STO) substrates (Shinkosha Co. Ltd., Japan) by pulsed laser deposition (PLD). The thin film catalysts were grown with a pulse repetition rate of 5 Hz at 650 °C and an oxygen partial pressure of 0.053 mbar.[19,36] The laser fluence was adapted for LSCO to 2.9 J cm^{-2} and for LSFO to 2.2 J cm^{-2}. The distance between the ceramic target and the heated substrate was 55 mm, while a nanosecond KrF-excimer laser with a wavelength of 248 nm was used to operate the PLD system.

Surface Analysis. The surface morphology of the thin film catalysts was investigated using a Cypher atomic force microscope (Asylum Research, Santa Barbara, United States) operated in tapping mode. AFM tips (PPP-NCHR, Nano-World AG, Switzerland) with a nominal tip radius of curvature below 10 nm have been employed.

Crystal Structure Analysis. The crystal structure of the thin film catalysts was characterized by X-ray diffraction (XRD, D8 Discover, Bruker AXS GmbH, Germany) by symmetric 2θ-ω scans. The diffractometer was equipped with a Goebel mirror, a monochromizedCu anode for $K_{\alpha 1}$ radiation with a wavelength of 1.54 Å.

Electronic Structure Analysis. NEXAFS measurements were performed at IQMT's soft X-ray beamline WERA at the KIT Light Source KARA (Karlsruhe, Germany). NEXAFS measurements at the Co $L_{2,3}$, Fe $L_{2,3}$, and O K-edges were carried out simultaneously in fluorescence yield (FY) and total electron yield (TEY) detection mode. After correction for photon flux variations and for the background, the spectra were normalized at the edge jump. The photon-energy resolution in the spectra was set to 0.2−0.4 eV. Photon energy calibration was ensured by adjusting the Ni L_3 peak position measured on a NiO single-crystal before and after each NEXAFS scan to the established peak position.

Electrochemical Characterization. Electrochemical characterization of the thin-film electrodes was performed using a rotating disc electrode (RDE) setup (Pine Research) in an oxygen-saturated 0.1 M KOH solution. The rotation rate was maintained at 1600 rpm, and a custom-made adapter constructed from PEEK was used for thin-film samples measuring 0.5 × 10 × 10 mm^3. The electrochemical cell consisted of a chemically inert Teflon beaker, the electrolyte, and a standard three-electrode setup. The electrolyte was prepared by dissolving KOH pellets (Sigma-Aldrich, 99.99%) in deionized water (Milli-Q, >18.2 MΩ cm). The solution was continuously purged with oxygen 30 min before and during the experiment to enhance its performance. A potentiostat (BioLogic SP-150, BioLogic Science Instruments, France) was connected to the thin-film samples at the backside and edges using a platinum contact applied via a platinum stamp. The thin-film catalysts served as the working electrode, while a platinum coil was used as the counter electrode. To isolate the center of the perovskite catalyst from the platinum contacts, an O-ring with a diameter of 7.5 mm was employed. For measurements, a Hg/HgO electrode (CHI Instruments) served as the reference electrode, calibrated to the RHE (HydroFlex) for each batch of electrolyte. The electrochemical testing included electrochemical impedance spectroscopy, scan-rate-dependent cyclic voltammetry in the pseudocapacitive redox phase change region, and cyclic voltammetry in the potential region for the OER, carried out over two successive cycles. After the electrochemical characterization, the samples were dried with a paper towel, which absorbed the residual electrolyte.

***In-Operando* Atomic Force Microscopy.** Electrochemical atomic force microscopy (AFM) of the thin-film electrodes was performed in a home-built electrochemical cell made from chemically resistant Kel-F in 0.1 M KOH (Sigma-Aldrich, 99.99%) in deionized water (Milli-Q, >18.2 MΩ cm) using custom-cut 0.5 × 5 × 5 mm^3-sized thin-film samples. The potentiostat (BioLogic SP-300, BioLogic Science Instruments, France) was connected to the backside of the substrate via a Cu-wire. A Pt-wire and an Ag|AgCl-electrode (3.5 M KCl, DRIREF-2SH, World Precision Instruments GmbH, Friedberg, Germany) were used as counter and reference electrodes, respectively. Electrochemical testing was conducted by cyclic voltammetry with a sweep rate of 10 mV/s.

The surface morphology of the thin-film electrodes was investigated using AFM (Dimension Icon, Bruker, Santa Barbara) in contact mode operated with a cantilever with a nominal tip radius below 10 nm and spring constant of 0.12 N m^{-1}, being individually calibrated to determine the normal load (PPP-Cont, Nanosensors, Switzerland). Gwyddion software was used to flatten (polynomial fit first order) topography images. Occasional error lines were removed from the image using a mask and removing the scan line error function.[39]

■ ASSOCIATED CONTENT

Supporting Information

The Supporting Information is available free of charge at https://pubs.acs.org/doi/10.1021/acscatal.5c02273.

> Electrochemical impedance spectroscopy, uncompensated resistance of the electrochemical cell, maximum current density over time, cyclic voltammetry, Co $L_{2,3}$, Fe $L_{2,3}$ and O K NEXAFS spectra (PDF)

■ AUTHOR INFORMATION

Corresponding Author

Anton Kaus − *Peter Grünberg Institute 7 (PGI-7), Forschungszentrum Jülich GmbH, 52428 Jülich, Germany;* orcid.org/0009-0004-0070-1795; Email: a.kaus@fz-juelich.de

Authors

Bixian Ying − *Münster Electrochemical Energy Technology (MEET), University of Münster, 48149 Münster, Germany*

Zhenjie Teng − *Münster Electrochemical Energy Technology (MEET), University of Münster, 48149 Münster, Germany*

Muzaffar Maksumov − *Institute of Energy Technologies 1 (IET-1), Forschungszentrum Jülich GmbH, 52428 Jülich, Germany; RWTH Aachen University, Institute of Physical Chemistry, 52074 Aachen, Germany*

Lisa Heymann − *Peter Grünberg Institute 7 (PGI-7), Forschungszentrum Jülich GmbH, 52428 Jülich, Germany;* orcid.org/0000-0002-0207-7840

Michael Merz − *Institute for Quantum Materials and Technologies (IQMT), Karlsruhe Institute of Technology (KIT), 76131 Karlsruhe, Germany; Karlsruhe Nano Micro Facility (KNMFi), KIT, 76131 Karlsruhe, Germany;* orcid.org/0000-0002-7346-7176

Stefan Schuppler − *Institute for Quantum Materials and Technologies (IQMT), Karlsruhe Institute of Technology (KIT), 76131 Karlsruhe, Germany; Karlsruhe Nano Micro Facility (KNMFi), KIT, 76131 Karlsruhe, Germany*

Peter Nagel − *Institute for Quantum Materials and Technologies (IQMT), Karlsruhe Institute of Technology (KIT), 76131 Karlsruhe, Germany; Karlsruhe Nano Micro Facility (KNMFi), KIT, 76131 Karlsruhe, Germany*

Florian Hausen − *Institute of Energy Technologies 1 (IET-1), Forschungszentrum Jülich GmbH, 52428 Jülich, Germany; RWTH Aachen University, Institute of Physical Chemistry, 52074 Aachen, Germany;* orcid.org/0000-0001-5712-6761

Karin Kleiner − *Münster Electrochemical Energy Technology (MEET), University of Münster, 48149 Münster, Germany;* Present Address: Centre Énergie, Matériaux et Télécommunications (EMT), Institut National de la Recherche Scientifique (INRS), Varennes, Quebec J3X1P7, Canada

Felix Gunkel − *Peter Grünberg Institute 7 (PGI-7), Forschungszentrum Jülich GmbH, 52428 Jülich, Germany*

Complete contact information is available at: https://pubs.acs.org/10.1021/acscatal.5c02273

Author Contributions

The manuscript was written through contributions of all authors. All authors have given approval to the final version of the manuscript.

Funding

This research was funded by the Deutsche Forschungsgemeinschaft (DFG, German Research Foundation)—project no. 493705276 as a part of the Priority Program SPP 2080 "Catalysts and reactors under dynamic conditions for energy storage and conversion."

Notes

The authors declare no competing financial interest.

■ ACKNOWLEDGMENTS

The authors acknowledge the KIT Light Source for providing beamtime at the WERA-beamline.

■ ABBREVIATIONS

OER, oxygen evolution reaction; LSCO, $La_{0.6}Sr_{0.4}CoO_{3-\delta}$; LSFO, $La_{0.6}Sr_{0.4}FeO_{3-\delta}$; AFM, atomic force microscopy; TM, transition metal; NEXAFS, near-edge X-ray absorption fine structure; XRD, X-ray diffraction; RHEED, reflection high-energy electron diffraction; Nb:STO, niobium-doped $SrTiO_3$; RMS, root-mean-square; RHE, reversible hydrogen electrode; CV, cyclic voltammogram; XAS, X-ray absorption spectroscopy; FY, fluorescence yield; TEY, total electron yield; OCP, open circuit potential; PLD, pulsed laser deposition

■ REFERENCES

(1) Tejuca, L. G.; Fierro, J. L. G.; Tascón, J. M. D. Structure and Reactivity of Perovskite-Type Oxides. In *Advances in Catalysis*; Elsevier, 1989; Vol. 36, pp 237−328.

(2) Peña, M. A.; Fierro, J. L. G. Chemical Structures and Performance of Perovskite Oxides. *Chem. Rev.* **2001**, *101* (7), 1981−2018.

(3) Chang, S. H.; Danilovic, N.; Chang, K.-C.; Subbaraman, R.; Paulikas, A. P.; Fong, D. D.; Highland, M. J.; Baldo, P. M.; Stamenkovic, V. R.; Freeland, J. W.; Eastman, J. A.; Markovic, N. M. Functional Links between Stability and Reactivity of Strontium

Ruthenate Single Crystals during Oxygen Evolution. *Nat. Commun.* **2014**, *5* (1), No. 4191, DOI: 10.1038/ncomms5191.

(4) Yang, C.; Rousse, G.; Svane, K. L.; Pearce, P. E.; Abakumov, A. M.; Deschamps, M.; Cibin, G.; Chadwick, A. V.; Corte, D. A. D.; Hansen, H. A.; Vegge, T.; Tarascon, J.-M.; Grimaud, A. Cation Insertion to Break the Activity/Stability Relationship for Highly Active Oxygen Evolution Reaction Catalyst. *Nat. Commun.* **2020**, *11* (1), No. 1378.

(5) Wohlgemuth, M.; Weber, M. L.; Heymann, L.; Baeumer, C.; Gunkel, F. Activity-Stability Relationships in Oxide Electrocatalysts for Water Electrolysis. *Front. Chem.* **2022**, *10*, No. 913419, DOI: 10.3389/fchem.2022.913419.

(6) Weber, M. L.; Gunkel, F. Epitaxial Catalysts for Oxygen Evolution Reaction: Model Systems and Beyond. *J. Phys. Energy* **2019**, *1* (3), No. 031001.

(7) Hwang, J.; Rao, R. R.; Giordano, L.; Katayama, Y.; Yu, Y.; Shao-Horn, Y. Perovskites in Catalysis and Electrocatalysis. *Science* **2017**, *358* (6364), 751−756.

(8) Vojvodic, A.; Nørskov, J. K. Optimizing Perovskites for the Water-Splitting Reaction. *Science* **2011**, *334* (6061), 1355−1356.

(9) Suntivich, J.; May, K. J.; Gasteiger, H. A.; Goodenough, J. B.; Shao-Horn, Y. A Perovskite Oxide Optimized for Oxygen Evolution Catalysis from Molecular Orbital Principles. *Science* **2011**, *334* (6061), 1383−1385.

(10) Man, I. C.; Su, H.-Y.; Calle-Vallejo, F.; Hansen, H. A.; Martínez, J. I.; Inoglu, N. G.; Kitchin, J.; Jaramillo, T. F.; Nørskov, J. K.; Rossmeisl, J. Universality in Oxygen Evolution Electrocatalysis on Oxide Surfaces. *ChemCatChem* **2011**, *3* (7), 1159−1165.

(11) Suntivich, J.; Hong, W. T.; Lee, Y.-L.; Rondinelli, J. M.; Yang, W.; Goodenough, J. B.; Dabrowski, B.; Freeland, J. W.; Shao-Horn, Y. Estimating Hybridization of Transition Metal and Oxygen States in Perovskites from O *K* -Edge X-Ray Absorption Spectroscopy. *J. Phys. Chem. C* **2014**, *118* (4), 1856−1863.

(12) Akbashev, A. R.; Roddatis, V.; Baeumer, C.; Liu, T.; Mefford, J. T.; Chueh, W. C. Probing the Stability of SrIrO $_3$ during Active Water Electrolysis *via Operando* Atomic Force Microscopy. *Energy Environ. Sci.* **2023**, *16*, 513−522, DOI: 10.1039/D2EE03704A.

(13) Cherevko, S. Stability and Dissolution of Electrocatalysts: Building the Bridge between Model and "Real World" Systems. *Curr. Opin. Electrochem.* **2018**, *8*, 118−125.

(14) Wan, G.; Freeland, J. W.; Kloppenburg, J.; Petretto, G.; Nelson, J. N.; Kuo, D.-Y.; Sun, C.-J.; Wen, J.; Diulus, J. T.; Herman, G. S.; Dong, Y.; Kou, R.; Sun, J.; Chen, S.; Shen, K. M.; Schlom, D. G.; Rignanese, G.-M.; Hautier, G.; Fong, D. D.; Feng, Z.; Zhou, H.; Suntivich, J. Amorphization Mechanism of SrIrO $_3$ Electrocatalyst: How Oxygen Redox Initiates Ionic Diffusion and Structural Reorganization. *Sci. Adv.* **2021**, *7* (2), No. eabc7323.

(15) Baeumer, C.; Li, J.; Lu, Q.; Liang, A. Y.; Jin, L.; Martins, H. P.; Duchon, T.; Gloss, M.; Gericke, S. M.; Wohlgemuth, M. A.; Giesen, M.; Penn, E. E.; Dittmann, R.; Gunkel, F.; Waser, R.; Bajdich, M.; Nemsak, S.; Mefford, J. T.; Chueh, W. C. Tuning Electrochemically Driven Surface Transformation in Atomically Flat LaNiO3 Thin Films for Enhanced Water Electrolysis. *Nat. Mater.* **2021**, *20* (5), 674−682.

(16) Heymann, L.; Weber, M. L.; Wohlgemuth, M.; Risch, M.; Dittmann, R.; Baeumer, C.; Gunkel, F. Separating the Effects of Band Bending and Covalency in Hybrid Perovskite Oxide Electrocatalyst Bilayers for Water Electrolysis. *ACS Appl. Mater. Interfaces* **2022**, *14* (12), 14129−14136.

(17) Akbashev, A. R.; Zhang, L.; Mefford, J. T.; Park, J.; Butz, B.; Luftman, H.; Chueh, W. C.; Vojvodic, A. Activation of Ultrathin $SrTiO_3$ with Subsurface $SrRuO_3$ for the Oxygen Evolution Reaction. *Energy Environ. Sci.* **2018**, *11* (7), 1762−1769.

(18) Baniecki, J. D.; Yamaguchi, H.; Harnagea, C.; Ricinschi, D.; Gu, Z.; Spanier, J. E.; Yamazaki, T.; Aso, H. Enhanced Stability and Thickness-Independent Oxygen Evolution Electrocatalysis of Heterostructured Anodes with Buried Epitaxial Bilayers. *Adv. Energy Mater.* **2019**, *9* (28), No. 1803846.

(19) Weber, M. L.; Baeumer, C.; Mueller, D. N.; Jin, L.; Jia, C.-L.; Bick, D. S.; Waser, R.; Dittmann, R.; Valov, I.; Gunkel, F. Electrolysis of Water at Atomically Tailored Epitaxial Cobaltite Surfaces. *Chem. Mater.* **2019**, *31* (7), 2337−2346.

(20) Weber, M. L.; Lole, G.; Kormanyos, A.; Schwiers, A.; Heymann, L.; Speck, F. D.; Meyer, T.; Dittmann, R.; Cherevko, S.; Jooss, C.; Baeumer, C.; Gunkel, F. Atomistic Insights into Activation and Degradation of La $_{0.6}$ Sr $_{0.4}$ CoO $_{3-\delta}$ Electrocatalysts under Oxygen Evolution Conditions. *J. Am. Chem. Soc.* **2022**, *144*, No. jacs.2c07226.

(21) Park, C. H.; Lee, H.; Choi, J.; Yun, T. G.; Lim, Y.; Bae, H. B.; Chung, S. Atomic-Level Observation of Potential-Dependent Variations at the Surface of an Oxide Catalyst during Oxygen Evolution Reaction. *Adv. Mater.* **2024**, *36* (38), No. 2403392.

(22) Mueller, D. N.; Machala, M. L.; Bluhm, H.; Chueh, W. C. Redox Activity of Surface Oxygen Anions in Oxygen-Deficient Perovskite Oxides during Electrochemical Reactions. *Nat. Commun.* **2015**, *6* (1), No. 6097.

(23) Merz, M.; Nagel, P.; Pinta, C.; Samartsev, A.; V Löhneysen, H.; Wissinger, M.; Uebe, S.; Assmann, A.; Fuchs, D.; Schuppler, S. X-Ray Absorption and Magnetic Circular Dichroism of LaCoO 3, La 0.7 Ce 0.3 CoO 3, and La 0.7 Sr 0.3 CoO 3 Films: Evidence for Cobalt-Valence-Dependent Magnetism. *Phys. Rev. B* **2010**, *82* (17), No. 174416.

(24) Hu, Z.; Wu, H.; Haverkort, M. W.; Hsieh, H. H.; Lin, H.-J.; Lorenz, T.; Baier, J.; Reichl, A.; Bonn, I.; Felser, C.; Tanaka, A.; Chen, C. T.; Tjeng, L. H. Different Look at the Spin State of Co 3 + Ions in a CoO 5 Pyramidal Coordination. *Phys. Rev. Lett.* **2004**, *92* (20), No. 207402.

(25) Risch, M.; Morales, D. M.; Villalobos, J.; Antipin, D. What X-Ray Absorption Spectroscopy Can Tell Us About the Active State of Earth-Abundant Electrocatalysts for the Oxygen Evolution Reaction**. *Angew. Chem., Int. Ed.* **2022**, *61* (50), No. e202211949.

(26) Tian, C.; Maheu, C.; Huang, X.; Oropeza, F. E.; Major, M.; Brötz, J.; Einert, M.; Donner, W.; Zhang, K. H.; Hofmann, J. P. Evaluating the Electronic Structure and Stability of Epitaxially Grown Sr-Doped $LaFeO_3$ Perovskite Alkaline O_2 Evolution Model Electrocatalysts. *RSC Appl. Interfaces* **2025**, *2* (1), 122−129.

(27) Abbate, M.; De Groot, F. M. F.; Fuggle, J. C.; Fujimori, A.; Strebel, O.; Lopez, F.; Domke, M.; Kaindl, G.; Sawatzky, G. A.; Takano, M.; Takeda, Y.; Eisaki, H.; Uchida, S. Controlled-Valence Properties of La 1 − x Sr x FeO 3 and La 1 − x Sr x MnO 3 Studied by Soft-x-Ray Absorption Spectroscopy. *Phys. Rev. B* **1992**, *46* (8), 4511−4519.

(28) Burton, A. R.; Paudel, R.; Matthews, B.; Sassi, M.; Spurgeon, S. R.; Farnum, B. H.; Comes, R. B. Thickness Dependent OER Electrocatalysis of Epitaxial LaFeO $_3$ Thin Films. *J. Mater. Chem. A* **2022**, *10* (4), 1909−1918.

(29) van der Minne, E.; Korol, L.; Krakers, L. M. A.; Verhage, M.; Rosário, C. M. M.; Roskamp, T. J.; Spiteri, R. J.; Biz, C.; Fianchini, M.; Boukamp, B. A.; Rijnders, G.; Flipse, K.; Gracia, J.; Mul, G.; Hilgenkamp, H.; Green, R. J.; Koster, G.; Baeumer, C. The Effect of Intrinsic Magnetic Order on Electrochemical Water Splitting. *Appl. Phys. Rev.* **2024**, *11* (1), No. 011420.

(30) Adiga, P.; Wang, L.; Wong, C.; Matthews, B. E.; Bowden, M. E.; Spurgeon, S. R.; Sterbinsky, G. E.; Blum, M.; Choi, M.-J.; Tao, J.; Kaspar, T. C.; Chambers, S. A.; Stoerzinger, K. A.; Du, Y. Correlation between Oxygen Evolution Reaction Activity and Surface Compositional Evolution in Epitaxial $La_{0.5}Sr_{0.5}Ni_{1-x}Fe_xO_{3-\delta}$ Thin Films. *Nanoscale* **2023**, *15* (3), 1119−1127.

(31) Wei, C.; Wang, Z.; Otani, K.; Hochfilzer, D.; Zhang, K.; Nielsen, R.; Chorkendorff, I.; Kibsgaard, J. Benchmarking Electrocatalyst Stability for Acidic Oxygen Evolution Reaction: The Crucial Role of Dissolved Ion Concentration. *ACS Catal.* **2023**, *13* (21), 14058−14069.

(32) Twight, L.; Tonsberg, A.; Samira, S.; Velinkar, K.; Dumpert, K.; Ou, Y.; Wang, L.; Nikolla, E.; Boettcher, S. W. Trace Fe Activates Perovskite Nickelate OER Catalysts in Alkaline Media via Redox-Active Surface Ni Species Formed during Electrocatalysis. *J. Catal.* **2024**, *432*, No. 115443.

(33) Tang, Y.; Chiabrera, F.; Morata, A.; Cavallaro, A.; Liedke, M. O.; Avireddy, H.; Maller, M.; Butterling, M.; Wagner, A.; Stchakovsky, M.; Baiutti, F.; Aguadero, A.; Tarancón, A. Ion Intercalation in Lanthanum Strontium Ferrite for Aqueous Electrochemical Energy Storage Devices. *ACS Appl. Mater. Interfaces* **2022**, *14* (16), 18486−18497.

(34) McDonnell-Worth, C.; MacFarlane, D. R. Ion Effects in Water Oxidation to Hydrogen Peroxide. *RSC Adv.* **2014**, *4* (58), 30551−30557.

(35) Exner, K. S. On the Mechanistic Complexity of Oxygen Evolution: Potential-Dependent Switching of the Mechanism at the Volcano Apex. *Mater. Horiz.* **2023**, *10* (6), 2086−2095.

(36) He, S.; Petracic, O.; Lauter, V.; Cao, L.; Zhou, Y.; Weber, M. L.; Schubert, J.; Concepción, O.; Dittmann, R.; Waser, R.; Brückel, T.; Gunkel, F. $La_{0.6}$ $Sr_{0.4}$ $CoO_{3-\delta}$ Films Under Deoxygenation: Magnetic And Electronic Transitions Are Apart from The Structural Phase Transition. *Adv. Funct. Mater.* **2024**, *34* (24), No. 2313208.

(37) Merz, M.; Fuchs, D.; Assmann, A.; Uebe, S.; V Löhneysen, H.; Nagel, P.; Schuppler, S. Spin and Orbital States in Single-Layered La 2 − x Ca x CoO 4 Studied by Doping- and Temperature-Dependent near-Edge x-Ray Absorption Fine Structure. *Phys. Rev. B* **2011**, *84* (1), No. 014436.

(38) Füngerlings, A.; Wohlgemuth, M.; Antipin, D.; van der Minne, E.; Kiens, E. M.; Villalobos, J.; Risch, M.; Gunkel, F.; Pentcheva, R.; Baeumer, C. Crystal-Facet-Dependent Surface Transformation Dictates the Oxygen Evolution Reaction Activity in Lanthanum Nickelate. *Nat. Commun.* **2023**, *14* (1), No. 8284.

(39) Nečas, D.; Klapetek, P. Gwyddion: An Open-Source Software for SPM Data Analysis. *Open Phys.* **2012**, *10* (1), 181−188.